POLITECNICO DI TORINO
Repository ISTITUZIONALE

Testing and modeling reinforced 3D concrete printing

Original
Testing and modeling reinforced 3D concrete printing / Tasaki, H., Kobayashi, N., Asakawa, T., Fantilli, A.P., Ding, Y., Egawa, R., Ohno, K., Nishiwaki, T.. - In: STRUCTURAL CONCRETE. - ISSN 1464-4177. - (2026), pp. 1-18. [10.1002/suco.70706]

Availability:
This version is available at: 11583/3013416 since: 2026-07-22T12:35:29Z

Publisher:
Wiley

Published
DOI:10.1002/suco.70706

Terms of use:

This article is made available under terms and conditions as specified in the corresponding bibliographic description in the repository

Publisher copyright

(Article begins on next page)

20 November 2026

Check for updates

Received: 1 February 2026 | Revised: 20 May 2026 | Accepted: 24 June 2026

DOI: 10.1002/suco.70706

ARTICLE

fib CEB-FIP WILEY

Testing and modeling reinforced 3D concrete printing

Haruto Tasaki[1] | **Noriyuki Kobayashi**[1] | **Tomoya Asakawa**[2] | **Alessandro P. Fantilli**[3] | **Yao Ding**[4] | **Ryo Egawa**[5] | **Kazunori Ohno**[6] | **Tomoya Nishiwaki**[7]

[1]Department of Architecture and Building Science, School of Engineering, Tohoku University, Sendai, Miyagi, Japan

[2]Technology Research Institute, Obayashi Corporation, Tokyo, Japan

[3]Department of Structural, Building and Geotechnical Engineering, Politecnico di Torino, Torino, Italy

[4]School of Civil Engineering, Chongqing University, Chongqing, China

[5]Graduate School of Information Science, Tohoku University, Sendai, Miyagi, Japan

[6]Tough Cyberphysical AI Research Center, Tohoku University, Sendai, Miyagi, Japan

[7]School of Engineering, Tohoku University, Sendai, Miyagi, Japan

Correspondence
Alessandro P. Fantilli, Department of Structural, Building and Geotechnical Engineering, Politecnico di Torino, Corso Duca degli Abruzzi 24, 10129 Torino, Italy.
Email: alessandro.fantilli@polito.it

Funding information
Japan Society for the Prmotion of Science KAKENHI, Grant/Award Number: JP23KF0004

Abstract

3D Concrete Printing (3DCP) provides several advantages, including construction productivity and sustainability, although the presence of cold joints reduces structural performance, particularly in zones subjected to tensile stresses. In addition, it is difficult to reinforce 3DCP structures with conventional steel rebars, generally used to reinforce concrete. To solve these problems, reinforcements are automatically inserted by means of a new system, in which pin-shaped reinforcement connects the concrete layers of traditional 3D printing (herein called R3DCP). To analyze the behavior of R3DCP beams, an experimental campaign has been performed and described in this paper. It includes material characterization, pullout tests to quantify the bond–slip between pin reinforcement and printed material, and full-scale four-point bending tests on 3DCP and R3DCP beams. Moreover, a new three-stage modeling approach, in which the contribution of discrete pin reinforcements is explicitly incorporated through a bond–slip equivalent constitutive relationship, is proposed. The good agreement between experimental findings and numerical results corroborates the effectiveness of the proposed reinforcing system, supporting future design guidelines for R3DCP.

KEYWORDS

cold joints, concrete layers, four-point bending test, pin reinforcement, pullout test, three-stage model

1 | INTRODUCTION

In recent years, 3D Concrete Printing (3DCP) has attracted a lot of attention due to the revolutionary technology introduced within the construction industry, where robots can automatize construction.[1] Indeed, 3DCP provides several advantages with respect to conventional construction methods, such as labor savings, improved productivity,[2] greater flexibility in building shapes,[3] and reduction of materials and components.[4–6]

The material extrusion method is one of the main printing procedures, as proved by research activities

This is an open access article under the terms of the Creative Commons Attribution License, which permits use, distribution and reproduction in any medium, provided the original work is properly cited.

© 2026 The Author(s). *Structural Concrete* published by John Wiley & Sons Ltd on behalf of International Federation for Structural Concrete.

devoted not only to the study of laminated materials,[7–10] but also to the development of standards[11–13] and practical applications.[14,15] On the other hand, the extrusion and lamination process produces discontinuities (interlayer cold joints) between the layers composing the final construction. As these discontinuities trigger crack growth, 3DCP structures inevitably exhibit lower structural integrity than traditional cast-in-situ components.[7,16] Due to the layer-by-layer deposition process, 3D printed concrete also shows anisotropic mechanical behavior, as strength and stiffness depend on the printing direction and layer orientation. This anisotropy is closely related to interlayer behavior and the formation of cold joints.[17] Moreover, in the zones where tensile stresses are expected, it is difficult to place conventional steel rebars before the lamination process, as in the case of conventional cast-in-situ and precast reinforced concrete (RC) structures.[18]

Several 3DCP structures were reinforced by laying mesh[19] or by inserting rebar directly between layers.[20–22] However, in both these reinforcing methods, labor-saving, and flexibility, which are the main advantages deriving from 3DCP, are lost due to the manual procedures needed to place the reinforcement.[19–22] Also, although the addition of fibers to concrete mixtures can improve the mechanical performance of the printed material, they provide a limited structural contribution across cold joints.[23–25]

Accordingly, a new device, which automatically inserts pin-shaped steel reinforcement (hereafter called "pin") orthogonally to the cold joints of concrete layers (or interlayers), was added to a 3DCP system.[26] In this new reinforced 3D concrete printing (R3DCP), manual labor can be completely eliminated[27,28] and strength and toughness of printed structure increase with respect to the traditional 3DCP.

Although the enhanced mechanical performances of pin-type or discrete reinforcement systems have been experimentally demonstrated in previous studies,[29] modeling approaches that quantitatively incorporate the contribution of inserted pins into the structural response of 3DCP elements remain limited. Hence, a study on 3DCP and R3DCP beams is described in the following sections. More precisely, the results of an experimental campaign performed on materials and structures are illustrated in Sections 2 and 3. A mechanical model is then introduced (Section 4) and finally validated by comparing experimental data and numerical predictions (Section 5). The findings of this investigation are expected to foster the use of R3DCP structural members and support the introduction of design guidelines.

2 | EXPERIMENTAL PROGRAMS

2.1 | R3DCP system and materials

The device capable of reinforcing 3D concrete elements is shown in Figure 1. With respect to a traditional *X*–*Y*–*Z* printer, composed of a 3DCP nozzle used to extrude concrete, an insertion system of steel pins similar to a staple gun is added (see Figure 1a).

The insertion system includes a cartridge from which the pins are pushed and inserted orthogonally into the laminated concrete.[26] The automatic R3DCP process consists of alternating the extrusion of laminated material and the insertion of pin reinforcements. The current printer enables the fabrication of concrete elements with the maximum volume of 0.36 m^3 (maximum height of 900 mm—*Z* direction, maximum width of 1000 mm—*X* direction, and maximum depth of 400 mm—*Y* direction).[22]

Figure 2a shows the geometrical properties of the pins used in the R3DCP system, and the results of tensile tests performed on bare pin. According to the stress–strain relationship of Figure 2b, the steel pins showed an elastic modulus $E_s = 210$ GPa, a yield strength measured with the 0.3% offset method $f_y = 700$ MPa, and an ultimate strength $f_u = 911$ MPa.

A commercially available thixotropic mortar, specifically designed for 3D printing, was employed. The target flow values, reached with the addition of water (14.75% by mass), were 110 ± 10 mm (0 stroke) and 140 ± 10 mm (15 strokes). The values of the main mechanical parameters of this mortar, measured with compressive tests on cylindrical specimens (diameter = 50 mm and height = 100 mm), are listed in Table 1.

The 3D printing process was executed according to the parameters listed in Table 2. These parameters were determined through preliminary printing trials in order to ensure stable extrusion, consistent layer formation, and repeatable reinforcement insertion. After printing one layer, the nozzle stopped extrusion, raised the position by 13 mm (*Z* direction), and resumed extrusion to laminate a new layer. In the presence of reinforcement, extrusion of the cement-based material was paused (at the end of a laminated layer) and the inserting mechanism was moved to a specific position. After completing the insertion of the pins, extrusion was resumed to print a new layer.

2.2 | H-shaped laminated beams

As shown in Figure 3a, two series of beams (see Table 3), with an H-shaped cross-section and composed of 69 layers

17517648, 0, Downloaded from https://onlinelibrary.wiley.com/doi/10.1002/suco.70706 by Politecnico Di Torino Sist. Bibl Del Polit Di Torino, Wiley Online Library on [30/07/2026]. See the Terms and Conditions (https://onlinelibrary.wiley.com/terms-and-conditions) on Wiley Online Library for rules of use; OA articles are governed by the applicable Creative Commons License

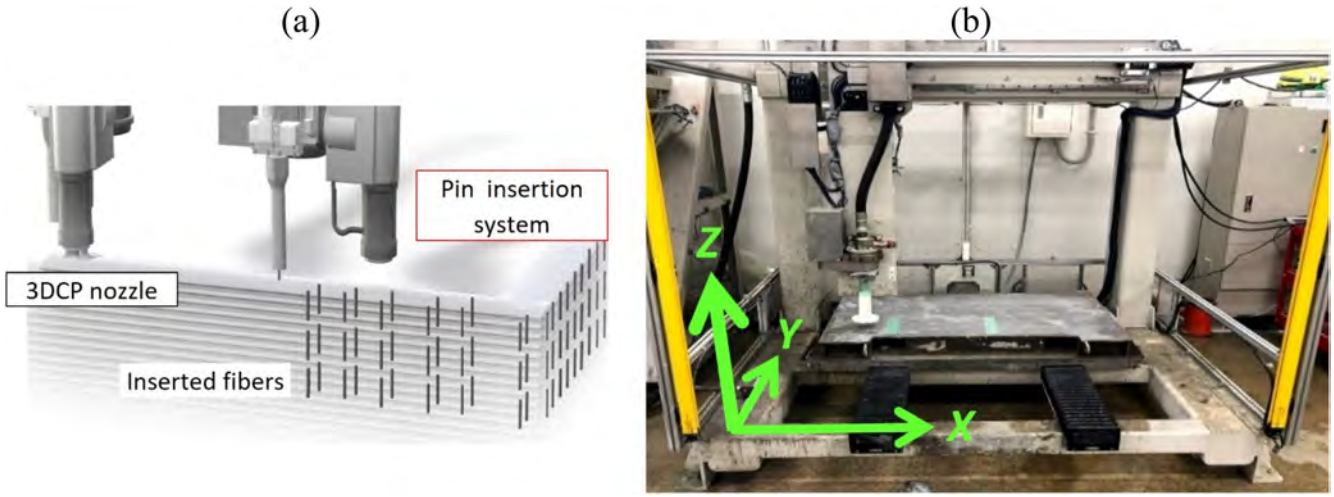


FIGURE 1 The reinforced 3D concrete printing (R3DCP) system used in this project: (a) traditional nozzle and reinforcing device; (b) the *X*–*Y*–*Z* movements of the printer.[22,26]

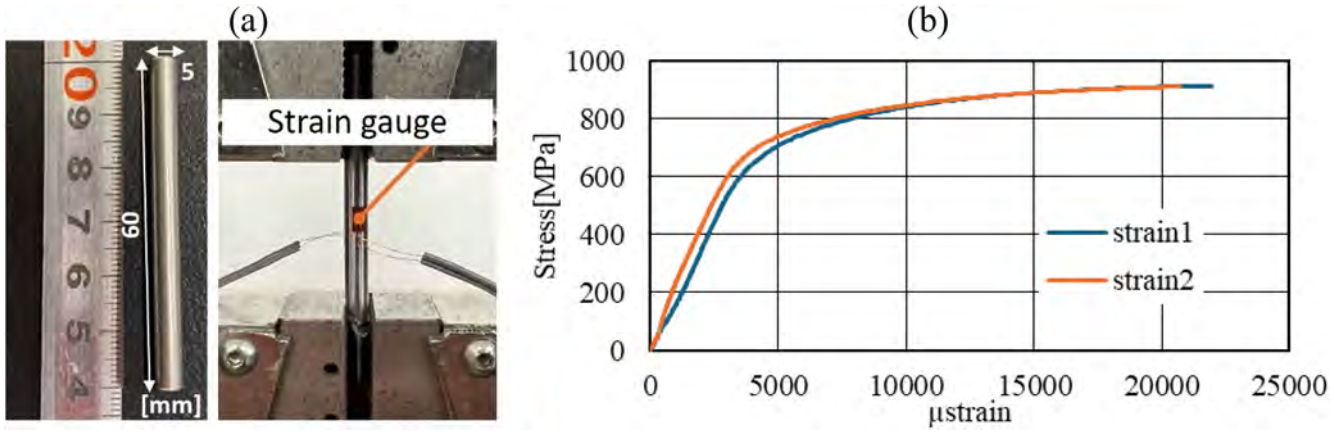


FIGURE 2 Characterization of reinforcement: (a) geometrical properties of the pins and setup of the tensile test; (b) stress–strain relationship of steel.

TABLE 1 Mechanical properties of the cement-based mortar used in the reinforced 3D concrete printing system.

Age (days)	f_c = compressive strength (MPa)	E_c = elastic modulus (GPa)
28	49.4 (SD = 1.02)	42.6 (SD = 0.26)
91	54.6 (SD = 0.77)	46.3 (SD = 1.01)

Abbreviation: SD, standard deviation.

TABLE 2 Lamination conditions of the cement-based mortar of 3D printer.

Conditions	Set value
Pump rotation speed (rpm)	100
Printing speed (mm/s)	80
Lamination width (mm)	35
Thickness of one layer (mm)	13
Speed at reinforcement insertion (mm/s)	80

(having a thickness of 13 mm), were printed and tested in four-point bending. The single beam of the H-N series was unreinforced, whereas the two beams of the H-SP series were reinforced with a total of 480 pins.

For a schematic visualization of reinforcement (Figure 3b), five color-coded sets were attributed to the pins. In the *X*–*Y* plane, each pin has eight distinct positions with respect to beam axis (*y* coordinate), whereas in the *Z* direction each pin crosses five layers. The five color-coded sets are shifted by one layer in the *Z* direction, forming a staggered overlapping arrangement, as summarized in Table 4. For instance, the blue pins connect layers 5–9, 10–14, 15–19, and so on, whereas the light-blue pins connect layers 6–10, 11–15, 16–20, and

17517648, 0, Downloaded from https://onlinelibrary.wiley.com/doi/10.1002/suco.70706 by Politecnico Di Torino Sist. Bibl Del Polit Di Torino, Wiley Online Library on [30/07/2026]. See the Terms and Conditions (https://onlinelibrary.wiley.com/terms-and-conditions) on Wiley Online Library for rules of use; OA articles are governed by the applicable Creative Commons License

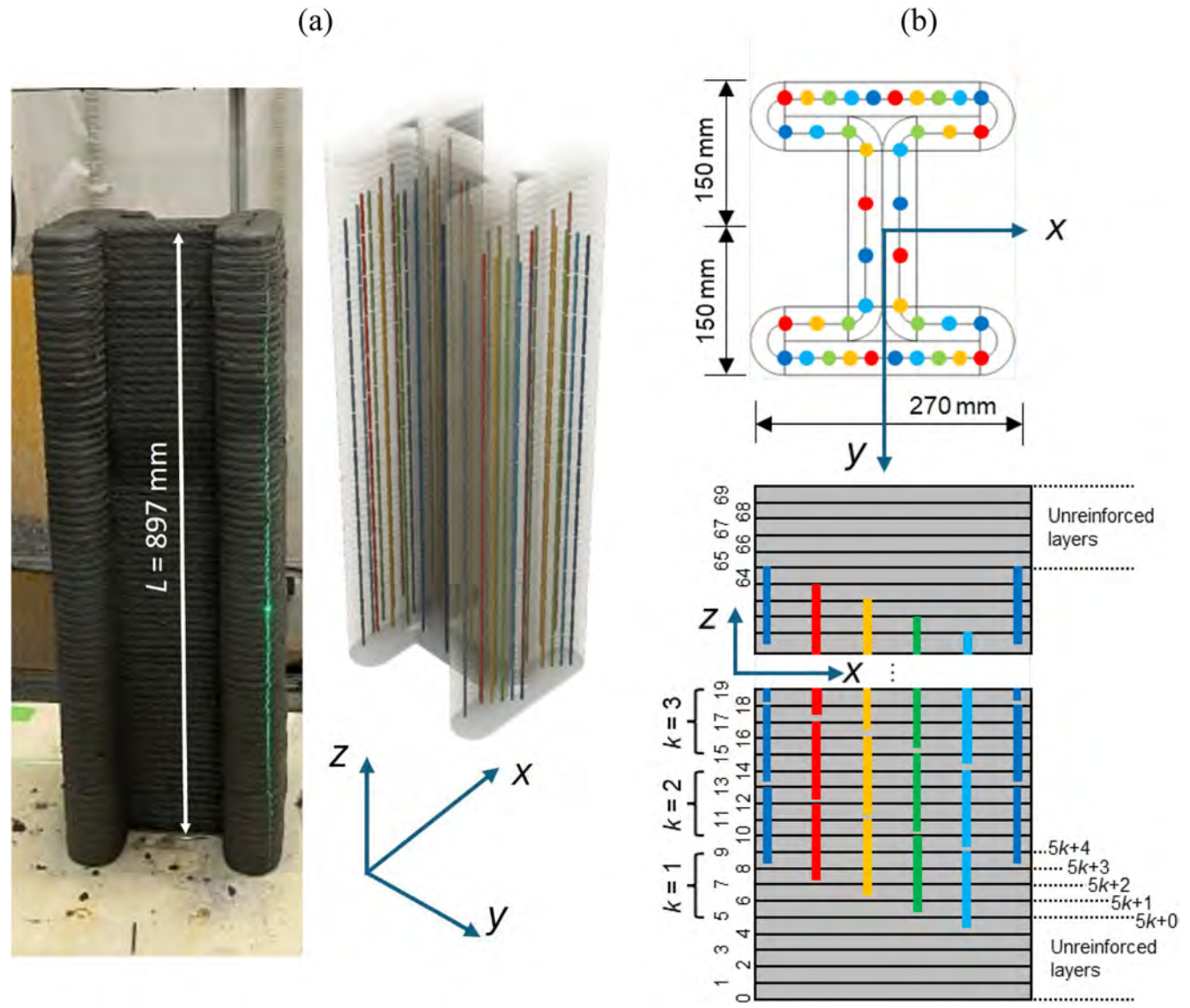


FIGURE 3 The beams printed in this research project: (a) illustration of the H-shaped beam; (b) arrangement of the pin reinforcements.

TABLE 3 The beams tested in this research project.

Series	Number of pins	Days of concrete curing
H-N-1	0	28
H-SP-1	480	28
H-SP-2		91

so on. Through this arrangement, the same number of reinforcements penetrated each layer. As a result, the reinforcement ratio (i.e., the ratio between the total cross-sectional area of the pins and that of the laminated material) was approximately 1% in each cross-section of the beam.

More precisely, the R3DCP process for the H-SP series consisted of the following steps, which describe how the layer arrangement shown in Figure 3b and Table 4 was achieved:

1. Start the extrusion and laminate the layers from 1 to 4, consecutively.
2. After laminating the $k = 1$ group of layers (i.e., from 5 to 9), insert the blue pins in 8 points of the X–Y plane.
3. After laminating the 10th layer (layer $5k + 0$, where $k = 2$), insert the light-blue pins in 8 points of the X–Y plane.
4. After laminating the 11th layer (layer $5k + 1$, where $k = 2$), insert green pins in 8 points of the X–Y plane.
5. After laminating the 12th layer (layer $5k + 2$, where $k = 2$), insert yellow pins in 8 points of the X–Y plane.

17517648, 0, Downloaded from https://onlinelibrary.wiley.com/doi/10.1002/suco.70706 by Politecnico Di Torino Sist. Bibl Del Polit Di Torino, Wiley Online Library on [30/07/2026]. See the Terms and Conditions (https://onlinelibrary.wiley.com/terms-and-conditions) on Wiley Online Library for rules of use; OA articles are governed by the applicable Creative Commons License

TABLE 4 Positions of pins within printed beams.

Color-coded set	Number of pins in the *X–Y* plane	Layers of insertion in the *Z* direction
Blue	8	5–9, 10–14, 15–19, 20–24, 25–29, 30–34, 35–39, 40–44, 45–49, 50–54, 55–59, 60–64
Light blue	8	6–10, 11–15, 16–20, 21–25, 26–30, 31–35, 36–40, 41–45, 46–50, 51–55, 56–60 ($5k + 1$)
Green	8	7–11, 12–16, 17–21, 22–26, 27–31, 32–36, 37–41, 42–46, 47–51, 52–56, 57–61 ($5k + 2$)
Yellow	8	8–12, 13–17, 18–22,23–27, 28–32, 33–37, 38–42, 43–47, 48–52, 53–57, 58–62 ($5k + 3$)
Red	8	9–13, 14–18, 19–23, 24–28, 29–33, 34–38, 39–43, 44–48, 49–53, 54–58, 59–63 ($5k + 4$)

6. After laminating the 13th layer (layer $5k + 3$, where $k = 2$), insert red pins in 8 points of the *X–Y* plane.
7. Repeat the steps from 2 to 6 by increasing k (up to $k = 12$) and reach the 64th layer. As the beams were cast vertically, to prevent the deformation of the laminated mortar of the first layers, the printing process is stopped for 30 min when the lamination height reached approximately 1/3 (when $k = 4$) and 2/3 (when $k = 8$) of the total height.
8. Finish the extrusion by laminating the layers from 65 to 69 without any reinforcement.

After printing, the beams remained within the printer for 1 day. Subsequently, they were wrapped with a plastic sheet to prevent moisture evaporation and cured for at least 28 days (see Table 3) at the laboratory condition (temperature = 20°C and RH = 50%).

2.3 | Tests setup

In the tensile zones of RC beams, the stiffness of uncracked concrete between two consecutive cracks (a phenomenon known as tension-stiffening) governs the mechanical response of RC structures, especially in the serviceability stage.[30] To model this mechanism in the proposed R3DCP beams, the pullout test illustrated in Figure 4 was carried out to measure the bond between the reinforcement and the laminated material.

Three specimens were prepared by inserting a pin within a cube (with a size of 40 mm) made with the cementitious mortar described in the previous section. One end of the pin was embedded into the concrete cube for a length of 30 mm (see Figure 4a). The unembedded part was clamped by the loading machine (Figure 4b). The pullout test was conducted at a displacement rate of 2.0 mm/min, with the upper side of the specimen restrained by a rigid steel plate. During the test, the applied force F and the apparent displacement between the pin and the cube (i.e., slip) were measured from the crosshead displacement of the testing machine and continuously recorded.

The beams illustrated in Figure 3, with and without steel pins, were tested in four-point bending 28 days (specimens H-N-1 and H-SP-1) and 91 days (specimen H-SP-2) after printing. Figure 5 shows the overview of the bending test performed by applying a displacement-controlled loading (with a rate of 0.3 mm/min to ensure quasi-static loading conditions) on a span of 750 mm (the third point length is 250 mm).

A load cell measured the total applied load P, whereas a linear variable differential transformer (LVDT) was also installed to independently measure the midspan deflections. In addition, eight strain gages (60 mm gage length) were glued to measure strains at different depths of the constant moment zones: two on the upper flange (edge in compression), three along the web sides, and three on the lower flange (edge in tension).

3 | EXPERIMENTAL RESULTS

The results of three pullout tests are reported in Figure 6 in terms of applied load F versus slip.

After an initial linear increment of the pullout load F with the slip (up to about 1660 N), a gradual decrement of F can be observed. It vanishes at slip = 30 mm, when it is equal to the initial embedded length. Nevertheless, just before the complete slippage of the pin, the pullout load increases due to the slight inclination of the pins. A similar phenomenon was observed and modeled by Fantilli et al.[31] in the case of inclined fibers within a cement-based matrix.

Figure 7a shows the load–deflection (P–η) curves of the four-point bending tests carried out on the three beams reported in Figure 3. In the absence of reinforcement (i.e., in the H-N-1 beam), the post-peak behavior is brittle, with a sudden decrement of the applied load immediately after the formation of the first crack. This crack initiated at an interlayer (the cold joint) within the constant moment zone, as shown in Figure 7b.

As illustrated in the same figure, failure of the reinforced H-SP-1 and H-SP-2 beams also seems to be dominated by a single flexural crack, although the softening branch of the P–η curves reveals a more ductile behavior

17517648, 0, Downloaded from https://onlinelibrary.wiley.com/doi/10.1002/suco.70706 by Politecnico Di Torino Sist. Bibl Del Polit Di Torino, Wiley Online Library on [30/07/2026]. See the Terms and Conditions (https://onlinelibrary.wiley.com/terms-and-conditions) on Wiley Online Library for rules of use; OA articles are governed by the applicable Creative Commons License

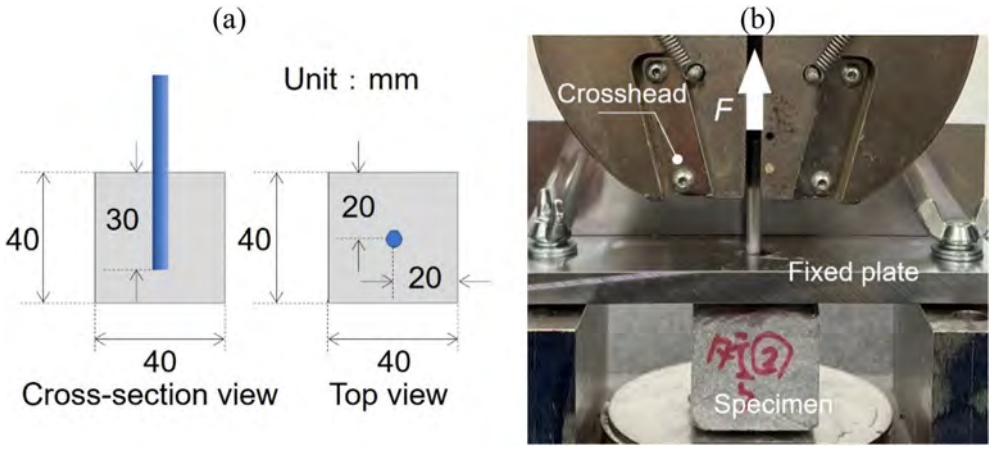


FIGURE 4 Pullout test on pin embedded into a cube specimen: (a) geometry of the samples; (b) pullout device used to perform the tests.

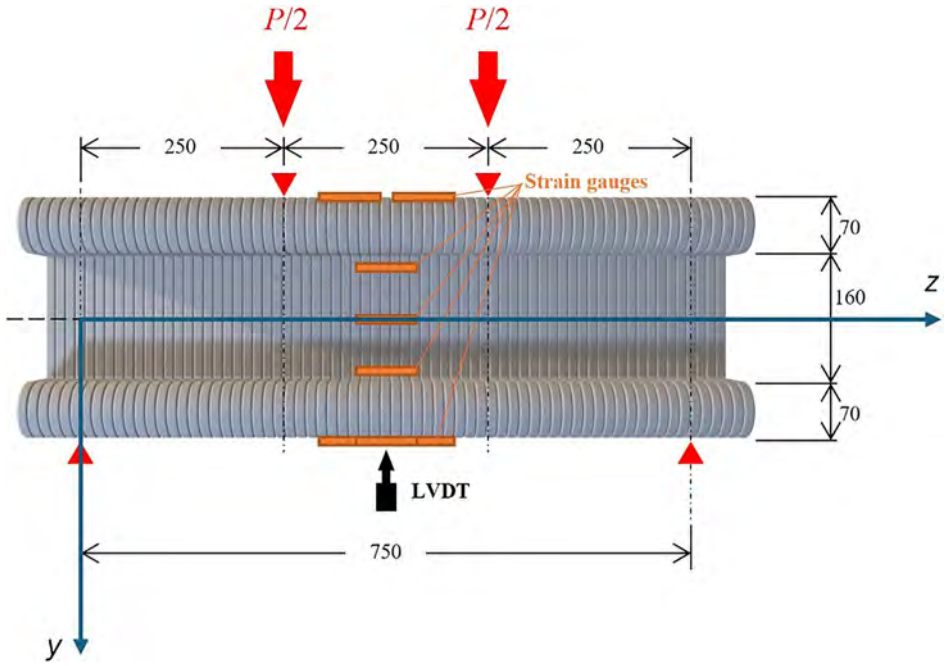


FIGURE 5 Four-point bending test on H-N and H-SP beams. LVDT, linear variable differential transformer.

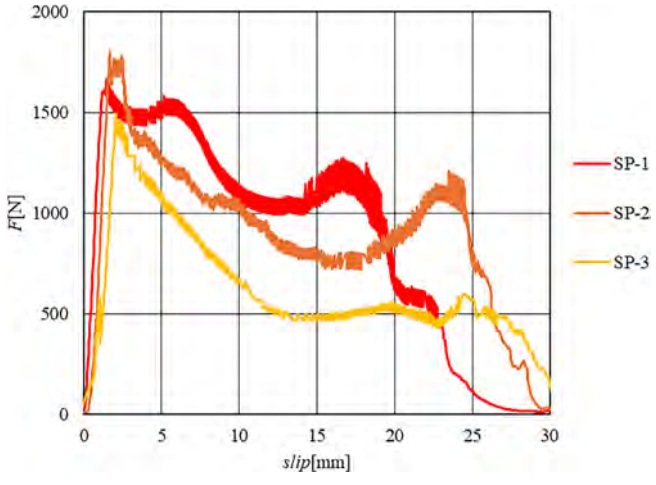


FIGURE 6 Results of the pullout tests.

than that of the H-N-1 beam. Indeed, steel pins tend to bridge the cracks as soon as they start to grow in the cold joints, which can be considered as preferential crack planes. As the pin is only a few times longer than the spacing between cold joints, they do not behave as continuous reinforcement over multiple cracks. Therefore, at large deflections, slippage of the pins tends to localize in one of the cold joints, and crack surfaces separate along one dominant crack in the H-SP-1 and H-SP-2 beams. Position and number of cracks may be influenced by geometrical properties, boundary conditions, and printing/casting procedure of the beams. Nevertheless, the dominant cracks appeared within the constant moment zone of all the beams, suggesting reasonably uniform structural behavior within the tested configuration.

17517648, 0, Downloaded from https://onlinelibrary.wiley.com/doi/10.1002/suco.70706 by Politecnico Di Torino Sist. Bibl Del Polit Di Torino, Wiley Online Library on [30/07/2026]. See the Terms and Conditions (https://onlinelibrary.wiley.com/terms-and-conditions) on Wiley Online Library for rules of use; OA articles are governed by the applicable Creative Commons License

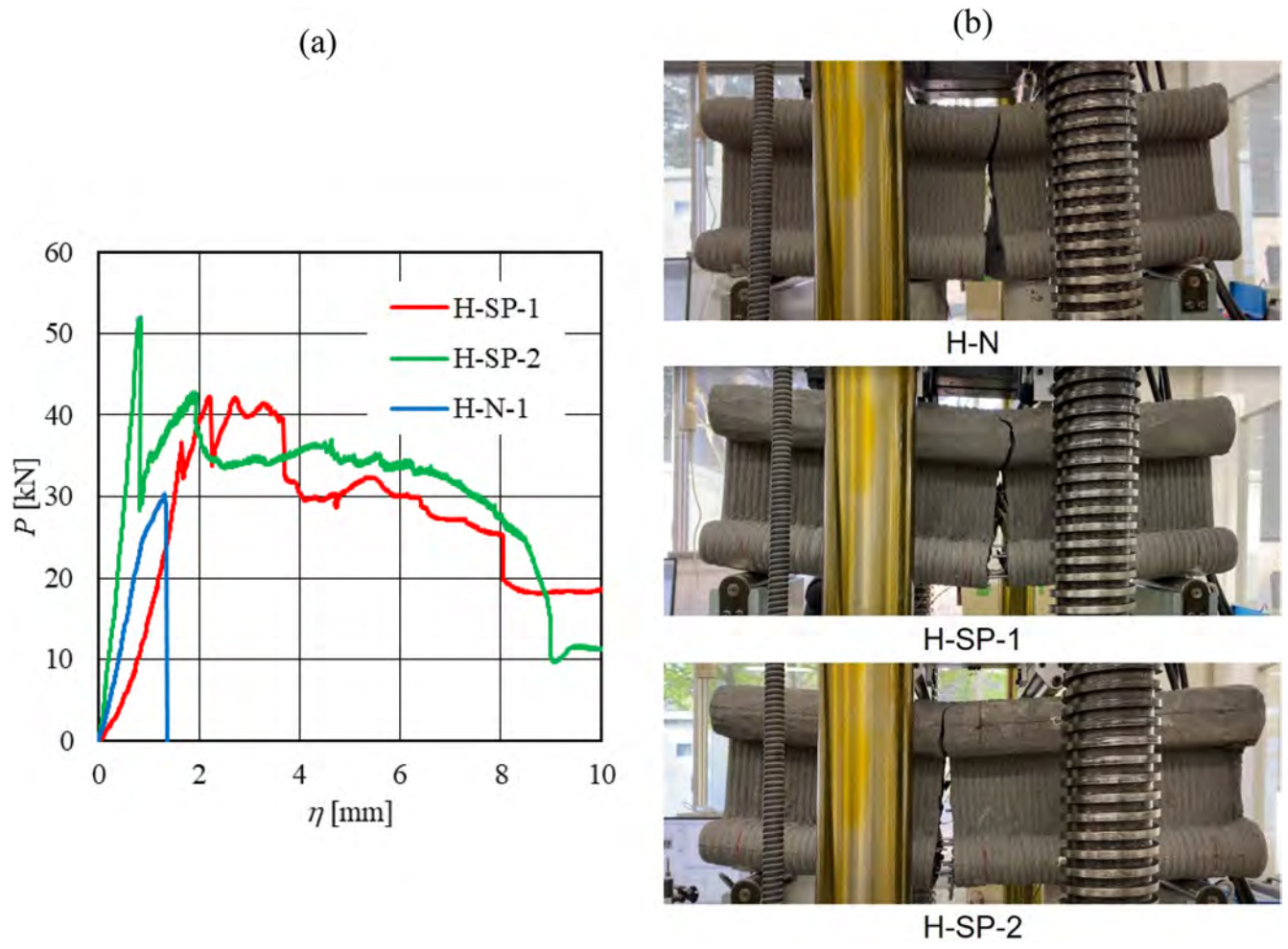


FIGURE 7 Results of four-point bending tests: (a) load–deflection curves; (b) pictures taken after the failure of the printed beams.

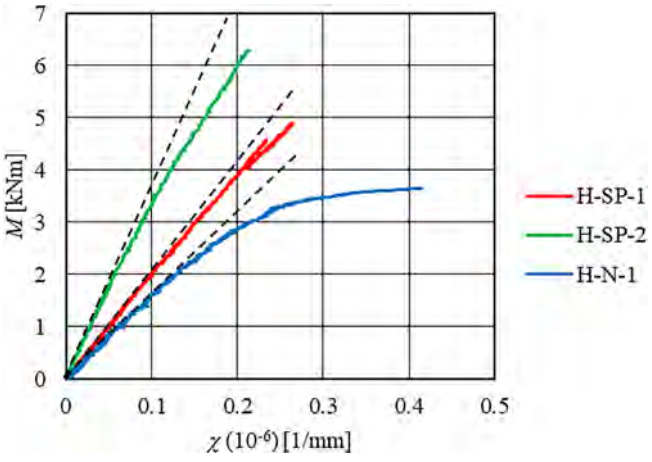


FIGURE 8 Moment–curvature diagrams experimentally measured through the strain gages located in the constant moment zone of the printed beams.

Focusing on the initial elastic phase of bending test, the moment–curvature (M–χ) diagrams depicted in Figure 8 were also obtained from the strains measured by the gages within the constant moment zone. All the beams exhibited an initial linear-elastic response, followed by a nonlinear stage after cracking. However, the whole post-peak behavior cannot be represented in terms of M–χ curves because strain gages progressively detached when strain localization began. Therefore, the post-peak branch cannot be observed in moment–curvature diagrams of Figure 8, which terminate when the last reliable curvature was measured.

The initial flexural stiffness of the reinforced beams (H-SP-1 and H-SP-2) was higher than that of the non-reinforced beam (H-N-1). This may be attributed to the presence of pins, which bridge the microcracks at the interlayers during the loading stage. However, the initial stiffness of H-SP-2 (tested after 91 days) is visibly higher than that of H-SP-1 (tested after 28 days), which is consistent with the increment of both compressive strength and elastic modulus of concrete with the time (see Table 1).

17517648, 0, Downloaded from https://onlinelibrary.wiley.com/doi/10.1002/suco.70706 by Politecnico Di Torino Sist. Bibl Del Polit Di Torino, Wiley Online Library on [30/07/2026]. See the Terms and Conditions (https://onlinelibrary.wiley.com/terms-and-conditions) on Wiley Online Library for rules of use; OA articles are governed by the applicable Creative Commons License

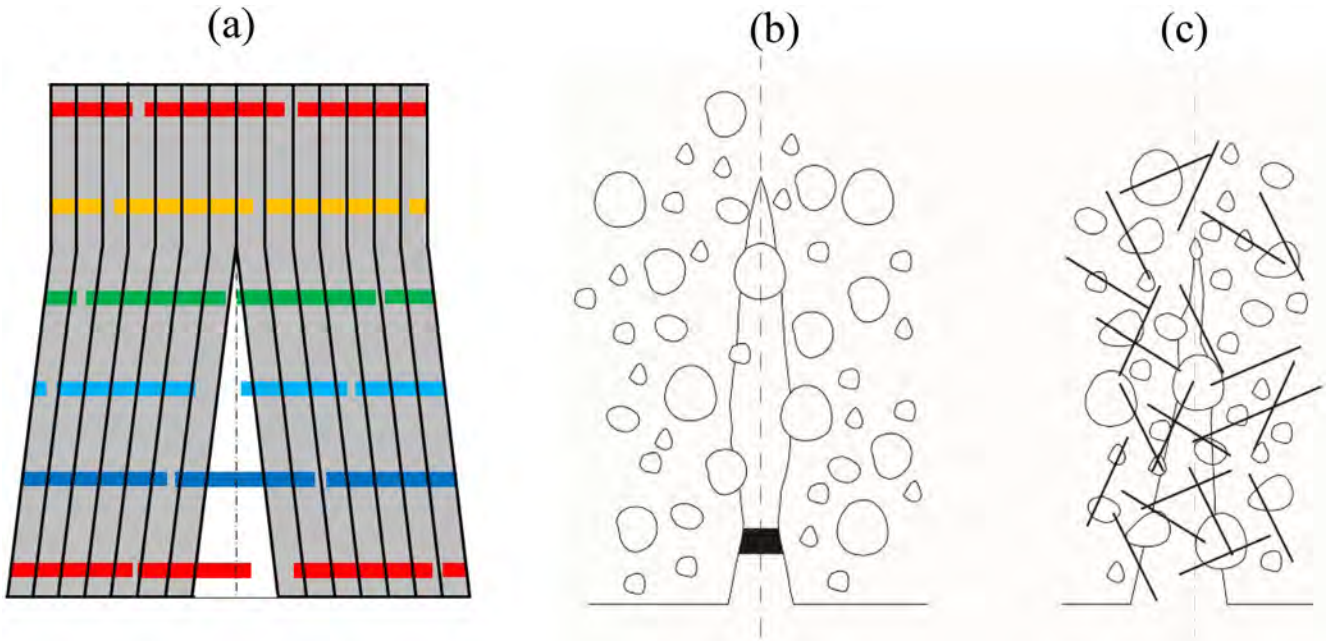


FIGURE 9 The bridging effect of reinforcement in concrete beams: (a) steel pins in the proposed reinforced 3D concrete printing; (b) traditional steel rebar in reinforced concrete; (c) steel fibers in fiber-reinforced concrete.

4 | MODELING 3D CONCRETE BEAMS WITH DISCONTINUOUS PINS

In the proposed R3DCP, the reinforcement with steel pins (Figure 9a) shows differences from and similarities to both traditional rebar in RC beams (Figure 9b) and fibers in fiber-reinforced concrete (FRC) beams (Figure 9c). Specifically, pins, rebar, and fibers tend to bridge the crack surfaces by transferring tensile stresses. In R3DCP beams, cracks typically initiate at the cold joints of the laminated layers and are restrained by the pins orthogonally to crack surfaces, similar to rebar in RC beams. However, pins are neither continuous (unlike rebar) nor randomly oriented (unlike fibers) within structural elements. Unlike traditional rebar, the length of the pins is comparable with the distance between cracks (or cold joints), similar to the fibers in FRC beams. Furthermore, the diameter of the pins (5 mm) is remarkably larger than that of fibers (typically less than 2 mm) and is comparable with the size of the standard reinforcing steel rebar. Consequently, neither the traditional theory of RC structures nor the approaches used for FRC,[32] can thoroughly model the R3DCP beams investigated herein.

More precisely, the constitutive laws of materials and tension-stiffening models are typically used to simulate RC beams in bending, where conventional steel rebar is significantly longer than crack spacing. This is not the case of the R3DCP beams analyzed herein because the length of the pins was only three to four times the distance between cold joints, where cracks localize. Since only a limited number of pins cross cold joints and cracks, it is not possible to include the bond between reinforcement and cementitious matrix within the stress–strain relationship of 3D printed concrete. Such an approach is only reasonable in FRC elements, where a vast number of fibers bridge the crack surfaces.

Hence, to effectively model the mechanical response of R3DCP beams in bending, the three-stage model proposed by Fantilli et al.[33] for RC beams has to be profoundly modified to consider the pullout response of the pins, in addition to the stress–strain relationships of concrete and steel. Based on these relationships, a new structural model, consisting of the sequential stages described in the following sections, is introduced for R3DCP beams.

4.1 | Stage I: The equivalent constitutive relationship of steel pins

To model the reinforcing pins, two different situations must be considered. In the uncracked stage (Figure 10a), the behavior of steel pins can be solely reproduced by the stress–strain relationship of steel (Figure 2b), as the perfect bond condition is assumed across the interlayers (full embedded stage). This assumption should be regarded as a model simplification for the initial uncracked stage. Similar idealizations are commonly used in tension-stiffening models, where crack width is related to the slip

17517648, 0, Downloaded from https://onlinelibrary.wiley.com/doi/10.1002/suco.70706 by Politecnico Di Torino Sist. Bibl Del Polit Di Torino, Wiley Online Library on [30/07/2026]. See the Terms and Conditions (https://onlinelibrary.wiley.com/terms-and-conditions) on Wiley Online Library for rules of use; OA articles are governed by the applicable Creative Commons License

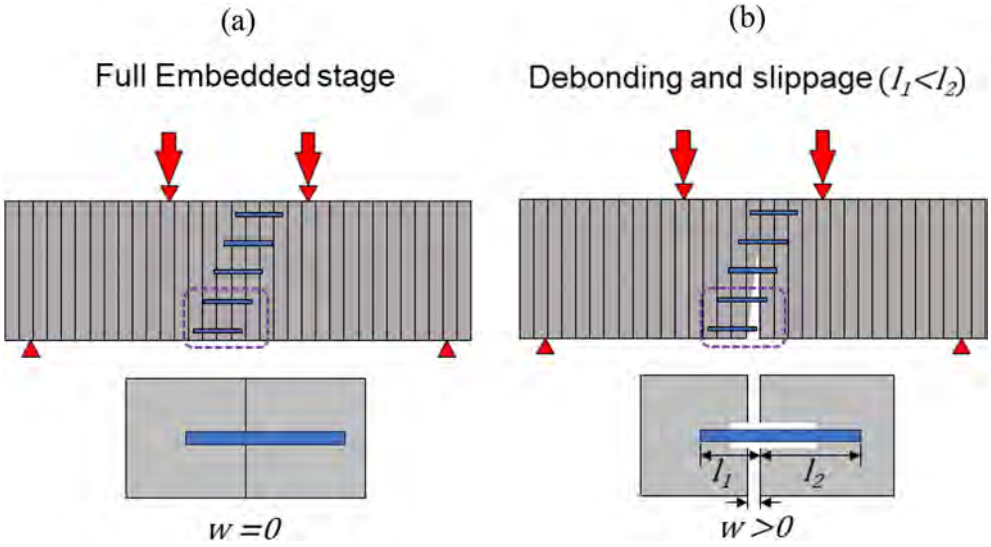


FIGURE 10 Behavior of pin reinforcements before (a) and after (b) cracking.

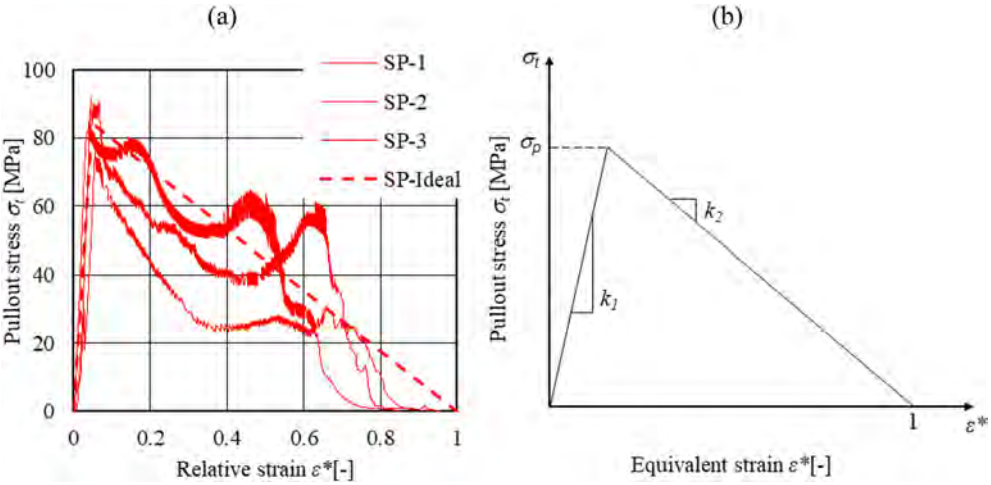


FIGURE 11 The equivalent constitutive relationship of the pin: (a) stress-equivalent strain from the pullout test; (b) ideal s_t–ε* relationship.

between steel and concrete.[30,32] In the present model, before the growth of a crack, no explicit slip is introduced between the pins and the surrounding mortar. Thus, pins are assumed to deform compatibly with the printed material.

However, as soon as a crack develops at an interlayer (Figure 10b), and the crack width w becomes larger than zero, a partial interaction between pins and laminated concrete initiates. This interaction, characterized by the slip between pin and the surrounding matrix, is governed by the pullout response depicted in Figure 6.

In the proposed model for R3DCP, a stress σ_t versus equivalent strain ε* is introduced (Figure 11). The stress is computed as follows:

$$\sigma_t = \frac{F}{A_p}, \tag{1}$$

where F = applied load in the pullout test; and A_p = cross-sectional area of the pin.

The equivalent strain ε* includes the contribution of the elastic deformation of the steel and the relative displacement between the pin and the surrounding concrete. It is worth noting that, due to the limited length of the pins, steel pins do not reach plastic strains before the complete slippage occurs. As both these contributions are included in the slip measured during the pullout tests of Figure 6, the equivalent strain ε* can be computed as follows:

$$\varepsilon^* = \frac{\text{slip}}{l_e}, \tag{2}$$

where l_e = embedded length of the pin (it is equal to 30 mm in Figure 4). By means of Equations (1 and 2), it is possible obtain the σ_t–ε* curves depicted in Figure 11a, starting from F–slip diagram reported in Figure 6.

The proposed σ_t–ε* relationship is introduced as an equivalent constitutive relationship for the pin reinforcement. Therefore, σ_t should be interpreted as nominal

17517648, 0, Downloaded from https://onlinelibrary.wiley.com/doi/10.1002/suco.70706 by Politecnico Di Torino Sist. Bibl Del Polit Di Torino, Wiley Online Library on [30/07/2026]. See the Terms and Conditions (https://onlinelibrary.wiley.com/terms-and-conditions) on Wiley Online Library for rules of use; OA articles are governed by the applicable Creative Commons License

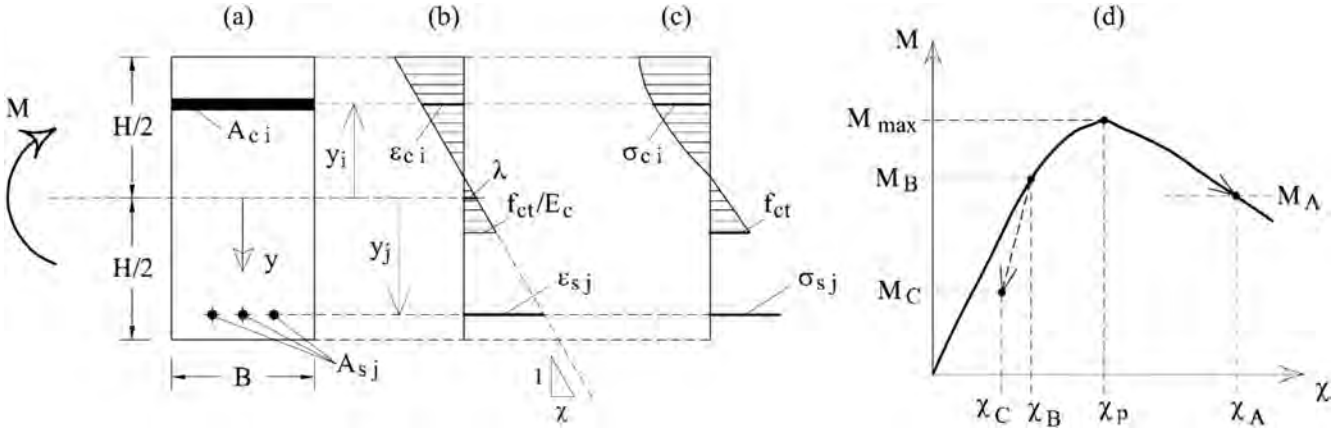


FIGURE 12 Computing the moment–curvature relationship in reinforced concrete beams: (a) cross-section of the beam; (b) state of strain; (c) state of stress; and (d) M–χ relationship.

equivalent tensile parameters used to represent the bond-controlled pullout response, rather than as the actual tensile stress acting on the pin cross-section. Similarly, ε^* is an equivalent strain parameter that includes both the elastic deformation of the steel pin and the relative displacement between the pin and the surrounding mortar. In other words, the σ_t–ε^* relationship implicitly accounts for the interaction along the contact surface governing the pullout response.

It is possible to simplify all the σ_t–ε^* curves with the ideal bilinear relationship shown in Figure 11b. In the ascending branch, the pullout stress increases linearly with the equivalent strain up to the peak (σ_p). In the subsequent descending branch, stress decreases till the complete slippage of the pin, which occurs at $\varepsilon^* = 1$. Based on the results of the pullout tests, the following parameters can be used: $\sigma_p = 84.27$ MPa (average peak stress of three specimens), $k_1 = 1789$ MPa (slope of the ascending branch), and $k_2 = -88.44$ MPa (slope of the descending branch). The nominal equivalent stress σ_p obtained from the pullout response is much lower than the tensile strength of the steel pin shown in Figure 2b. This indicates that the steel pin is far from failure and does not reach yield or plastic deformation. On the contrary, the contribution of the pins is mainly ruled by the slippage of the steel pin with respect to the surrounding printed material.

4.2 | Stage II: Moment–curvature relationship

Similar to RC structures, the second stage consists of computing the moment–curvature relationship.[30] In the beams investigated herein, with normal force $N = 0$ and the bending moment within the [Y–Z] plane of the beam, the so-called stripe model can be adopted. In a cross-section of the beam, the area of concrete is divided into n stripes parallel to the X axis (Figure 12a), having an area A_{ci}. In each point of the stripe, material properties, strain ε_{ci} (Figure 12b) and stress σ_{ci} (Figure 12c) are constant. Similarly, for each reinforcement layer having a cross-sectional area A_{sj}, a single value for both the stress σ_{sj} and the strain ε_{sj} can be assumed.

By neglecting the shear contribution to deformation and assuming that plane sections remain plane after deformation, the linear strain profile is defined by the parameters χ (curvature) and λ (strain at $y = 0$). If the constitutive relationships of materials are known, the moment–curvature relationship (M–χ) of Figure 12d can be computed with the following numerical procedure:

1. Impose the curvature χ in the cross-section (Figure 12d).
2. Assume a trial value for λ.
3. Compute the state of strain in the n concrete stripes, and in the m reinforcement layers:

$$\varepsilon_{ci} = \lambda + \chi \times y_i \quad (i = 1, 2, \ldots n). \tag{3a}$$

$$\varepsilon_{sj} = \lambda + \chi \times y_j \quad (j = 1, 2, \ldots m). \tag{3b}$$

4. From the stress–strain relationship of materials, the state of stress is defined in both concrete (σ_{ci}) and steel (σ_{sj}), as shown in Figure 12c.
5. If the equilibrium to translation is not satisfied, that is

$$N = \int_A \sigma \, dA = \sum_{i=1}^{n} \sigma_{ci} \times A_{ci} + \sum_{j=1}^{m} \sigma_{sj} \times A_{sj} \neq 0, \tag{4}$$

Change the value of λ and go back to Step 3.

17517648, 0, Downloaded from https://onlinelibrary.wiley.com/doi/10.1002/suco.70706 by Politecnico Di Torino Sist. Bibl Del Polit Di Torino, Wiley Online Library on [30/07/2026]. See the Terms and Conditions (https://onlinelibrary.wiley.com/terms-and-conditions) on Wiley Online Library for rules of use; OA articles are governed by the applicable Creative Commons License

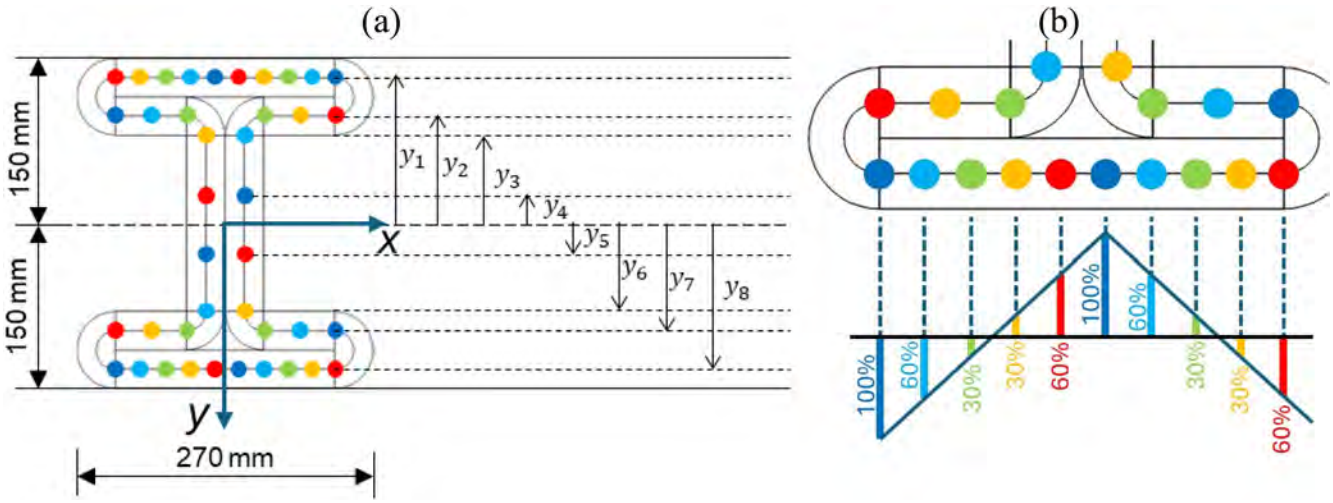


FIGURE 13 Steel pins in the reinforced 3D concrete printing beams: (a) depths of pin reinforcements with respect to the X axis; (b) efficiency of the pins at the bottom of the beam (y_8).

6. When $N = 0$, compute the bending moment M corresponding to the curvature χ with the following equation:

$$M = \int_A \sigma \times y \, dA = \sum_{i=1}^{n} \sigma_{ci} \times y_i \times A_{ci} + \sum_{j=1}^{m} \sigma_{sj} \times y_j \times A_{sj}. \tag{5}$$

If the previous procedure is repeated for all the possible curvatures, the whole M–χ of Figure 12d can be obtained.

The above calculation of M–χ is valid in the case of perfect bond between concrete and reinforcement, which occurs in the absence of cracks. In the cracked H-SP beams investigated herein, due to the small length of the steel pins, which have a partial interaction with the laminated concrete, the previous procedure needs to be modified. Firstly, the stress–strain relationship shown in Figure 11 must be attributed to the eight layers ($m = 8$) of the pins depicted in Figure 13a. However, due to the diagonal pattern of reinforcement (Figure 3), the pins on the same reinforcement layer (or at the same depth y_j of each cross-section) do not have the same efficiency. For instance, in the 10 pins on the bottom of the H-shaped R3DCP beam ($j = 8$ in Figure 13b), the pullout resistance depends on the shortest embedded length of the pin shown in Figure 10b. When the embedded lengths are the same on both sides of the cracked cross-section ($l_1 = l_2 = 30$ mm), the pin is assumed to achieve the maximum efficiency (100%).

At the same reinforcement depth, when pins are shifted by one or more layers, the embedded lengths are not the same ($l_1 \neq l_2$ in Figure 10b) and the efficiency reduces. For the sake of simplicity, the ratio between the shortest embedded length and the potential maximum embedded length (i.e., half of the total length of the pin) is herein assumed to quantify reinforcement efficiency.

TABLE 5 Efficiency of pin reinforcements.

Color coding	Minimum embedded length (mm)	Efficiency
Blue	30	100%
Light blue	18	60%
Green	9	30%
Yellow	9	30%
Red	18	60%
Blue	30	100%

Starting from the blue pin on the left of the eighth reinforcing layer (y_8 in Figure 13b), the maximum efficiency (100%) is restored after five pins (i.e., in the next blue pin), whereas the pins in between, with shorter embedded lengths, exhibit reduced efficiency. They are 60% and 30% for the minimum embedded lengths of 18 mm (in light blue and red pins) and 9 mm (in green and yellow pins), respectively. These efficiency values, also reported in Table 5, are defined according to the shortest embedded length of the pins across the cracked interface. When the shortest embedded length is 30 mm, the maximum efficiency of 100% is assigned. For shorter embedded lengths of 18 and 9 mm, the efficiency factors are taken as 60% and 30%, respectively, assuming that the load transfer contribution is proportional to the shortest embedded length. Accordingly, at the same distance from the neutral axis of a beam in bending, not all the pins provide the maximum contribution. Thus, a reduction factor ψ_j is

17517648, 0, Downloaded from https://onlinelibrary.wiley.com/doi/10.1002/suco.70706 by Politecnico Di Torino Sist. Bibl Del Polit Di Torino, Wiley Online Library on [30/07/2026]. See the Terms and Conditions (https://onlinelibrary.wiley.com/terms-and-conditions) on Wiley Online Library for rules of use; OA articles are governed by the applicable Creative Commons License

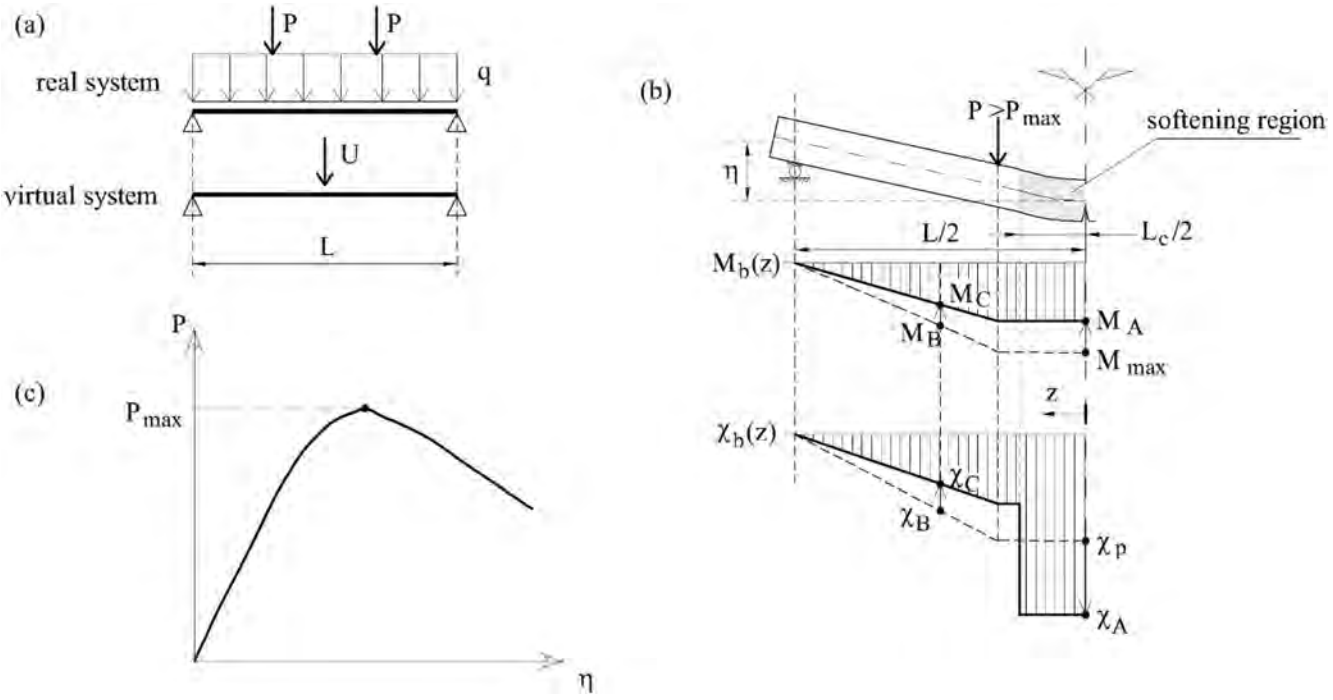


FIGURE 14 Evaluating the load–deflection P–η diagram of a beam in bending: (a) loads acting on the virtual and real systems; (b) distributions of curvature and bending moment in the real system; (c) final shape of the P–η diagram.

introduced as a weighted average of the contributions of the pins located at the same reinforcement depth.

In general, at the j-th reinforcement layer, a reduction factor ψ_j for the pin contribution can be computed:

$$\psi_j = \frac{100\% \times n_1 + 60\% \times n_2 + 30\% \times n_3}{n_1 + n_2 + n_3}, \tag{6}$$

where n_1, n_2, and n_3 = number of the pins, at the depth y_j, having an efficiency of 100%, 60%, and 30%, respectively. Accordingly, the equilibrium equations for RC beams (originally Equations (4 and 5)) are modified as follows: for R3DCP beams:

$$N = \int_A \sigma \, dA = \sum_{i=1}^{n} \sigma_{ci} \times A_{ci} + \sum_{j=1}^{m} \psi_j \times \sigma_{sj} \times A_{sj} \neq 0. \tag{7}$$

$$M = \int_A \sigma \times y \, dA = \sum_{i=1}^{n} \sigma_{ci} \times y_i \times A_{ci} + \sum_{j=1}^{m} \psi_j \times \sigma_{sj} \times y_j \times A_{sj}. \tag{8}$$

4.3 | Stage III: The load–deflection diagrams

In the statically determinate R3DCP beam depicted in Figure 5, once the M–χ relationship is established for all the cross-sections, the deflection η corresponding to the applied loads P can be evaluated with the virtual work equation. Based on the conservation of energy, the external work, defined as the product of external forces (acting on a virtual system—Figure 14a) and the external displacements (of the real system—Figure 14a), is equal to the internal strain energy of the beam. The latter is computed with the internal forces acting on the virtual system and the dual deformations of the real system. In other words:

$$\eta = \frac{1}{U} \int_0^L M_a(z) \times \chi_b(z) \, dz, \tag{9}$$

where U = load on the virtual system (dual of the midspan deflection η in real system); $M_a(z)$ = distribution of bending moment due to the virtual load U acting on the virtual system; $\chi_b(z)$ = distribution of curvature due to the external actions (self-weight q and loads P applied to the real system); L = length of the whole beam (Figure 14a).

The computation of the whole P–η diagram cannot be performed by increasing the external actions, because P could not be a monotonic function of η (see Figure 7). After reaching the maximum load P_{max}, a descending branch in the P–η diagram occurs due to the localization of curvatures (Figure 12d).

In the bending tests on R3DCP beams, when the main crack is supposed to occur in the midspan cross-

17517648, 0, Downloaded from https://onlinelibrary.wiley.com/doi/10.1002/suco.70706 by Politecnico Di Torino Sist. Bibl Del Polit Di Torino, Wiley Online Library on [30/07/2026]. See the Terms and Conditions (https://onlinelibrary.wiley.com/terms-and-conditions) on Wiley Online Library for rules of use; OA articles are governed by the applicable Creative Commons License

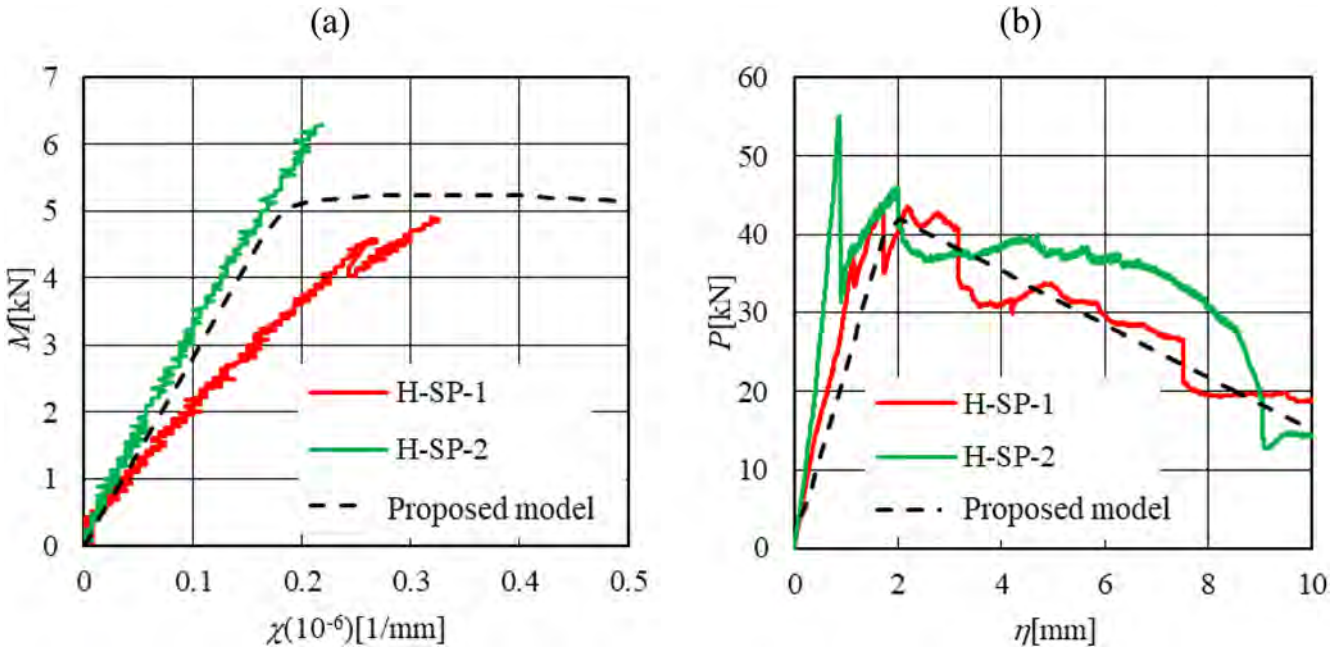


FIGURE 15 Comparing the experimental results measured on reinforced 3D concrete printing beams and the predictions of the three-stage model: (a) moment–curvature relationships; (b) load–deflection diagrams.

section (Figure 14b), a softening region can be defined within the constant moment zone,[34] whereas the rest of the beam undergoes elastic unloading. The post-peak branch of the P–η diagram is governed by this region, with a characteristic length L_c equal to the length of the pins, which transfer tensile stresses across the cracks of R3DCP in tension. As the result of this approach depends on beam geometry and pin configuration, L_c should be recalibrated when different pin lengths, reinforcement arrangements, or member geometries are considered.

To compute the function $\chi_b(z)$ of Equation (9), it is necessary to apply the following steps:

1. Select a curvature χ_A ($z = 0$) in the midspan cross-section of a four-point bending beam (Figure 14b).
2. Compute the bending moment M_A in the same cross-section (by means of the M–χ relationship of Figure 12d) and in all the cross-sections of the beam. From this distribution, the value of P can be obtained (in a statically determinate beam).
3. If $\chi_A \le \chi_p$ (where, χ_p = curvature at M_{max}), then the curvature distribution $\chi_b(z)$ is on the ascending branch of the M–χ relationship illustrated in Figure 12d;
4. If $\chi_A > \chi_p$, in the cross-sections at distance $z \le L_c/2$ the condition $\chi_b(z) = \chi_A$ is assumed; in the rest of the beam, curvature distribution $\chi_b(z)$ is obtained referring to the unloading branch of M–χ relationship (see the unloading from point B to C in Figures 12d and 14b).
5. By means of the Equation (9), the value of η can be computed

If the previous steps are repeated for all the possible curvatures of the midspan cross-section, the whole P–η diagram of the beams can be obtained (Figure 14c).

5 | COMPARING EXPERIMENTAL DATA AND NUMERICAL RESULTS

To evaluate the effectiveness of the predictive approach previously introduced, the numerical results obtained with the three-stage model are herein compared with the experimental data measured with the four-point bending tests on H-shaped R3DCP beams.

The first comparison is shown in Figure 15a, where the dashed curve represents the moment–curvature relationships computed with the model described in Section 4.2 and the material properties experimentally measured (see Section 2.1). The stress–strain relationship of concrete includes Sargin's parabola for the part in compression, up to the peak of compressive stress (f_c), and the linear part in tension before reaching the tensile strength f_{ct}.[32,35] In particular, $f_c = 52$ MPa (average values of those reported in Table 1), elastic modulus

17517648, 0, Downloaded from https://onlinelibrary.wiley.com/doi/10.1002/suco.70706 by Politecnico Di Torino Sist. Bibl Del Polit Di Torino, Wiley Online Library on [30/07/2026]. See the Terms and Conditions (https://onlinelibrary.wiley.com/terms-and-conditions) on Wiley Online Library for rules of use; OA articles are governed by the applicable Creative Commons License

$E_c = 44.5$ GPa, and tensile strength $f_{ct} = 3.87$ MPa (the latter values were estimated from f_c[35]).

The numerical M–χ curve appears in good agreement with those experimentally measured because the different stiffness may be attributed to the compressive strength (and elastic modulus) of concrete, which varies with the age (H-SP-1 was tested after 28 days, H-SP-2 was tested after 91 days). As the model is capable of representing the first elastic branch of M–χ, it effectively captures the initial linear-elastic behavior observed in the two tests performed on H-SP beams.

The global performance of the three-stage model is also shown in Figure 15b, where the load-deflection curves are compared. The prediction curve (dashed line) was computed by applying the principle of virtual work (see Section 4.3), in which the real curvatures are derived from the theoretical M–χ relationship. Although the difference in peak load between experimental and numerical results is approximately 0% for H-SP-1 and about 23% for H-SP-2, the model captures the main features of the experimental P–η diagram, including the initial stiffness and the post-peak response. The good agreement between the results of the theoretical model and the experimental data is a sort of validation of the proposed modeling approach. In particular, during the post-peak stage, the computed load-deflection curve successfully reproduces the effects of cracking (in the interlayer), and the pullout response of the pins crossing the crack. It corroborates both the assumptions that the ductility of R3DCP beams is governed by the pullout of pin reinforcements, modeled through the equivalent σ_t–ε^* relationship, and the reduction factor of Equation (6).

Furthermore, the results shown in Figure 15 support the effectiveness of the new proposed procedure, which lays the foundations for design-oriented modeling of R3DCP beams. Indeed, by changing the bond properties and the geometries of the steel pins, both σ_t–ε^* (which depends on the pullout behavior) and P–η (influenced by the characteristic length L_c of the softening region) can be updated while maintaining the same three-stage modeling framework.

Nevertheless, further tests are required to consider the model as a general design tool for different member geometries or reinforcement configurations, because R3DCP members may also be influenced by printing parameters, such as extrusion stability, layer geometry, printing speed, and the timing of pin insertion. All these factors affect both interlayer quality and the bond between pins and printed material. However, compared with mesh reinforcement or the insertion of rebar, the proposed pin reinforcing system has the advantage of directly connecting adjacent printed layers while maintaining the automated nature of the printing process. As the present study focuses on flexural members and on the tensile bridging contribution of pins, further investigations are required to also evaluate the influence of printing parameters, compare the proposed method with other reinforcement strategies, and to establish practical design and safety formats for different structural applications.

6 | CONCLUSIONS

Based on the results of the experimental and theoretical investigations previously described, the following conclusions can be drawn:

1. R3DCP is a new way of inserting reinforcement into 3D printed concrete layers. The pins used as reinforcement are in between the rebar of RC structures and the randomly distributed fibers of FRC beams.
2. Beams with H-shaped cross-sections and reinforced with steel pins exhibit superior ductility compared to the unreinforced specimen. This is due to the bridging mechanism provided by the pins crossing the cracks, which generally occur at the interlayers of 3D printed concrete, which effectively act as cold joints.
3. A new three-stage model can be used to predict the load-deflection diagram of statically determined R3DCP beams. In Stage 1, the equivalent stress–strain response of pins, which in turn depends on the pullout between pin and 3D printed concrete, is defined. From this response, a moment–curvature M–χ relationship is obtained in Stage 2. Finally, the load-deflection P–η curve of R3DCP beam is computed (Stage 3).
4. The computed M–χ relationship seems to capture the initial linear-elastic flexural stiffness measured during the tests on R3DCP beams, indicating the capability of the model to represent the elastic response. Furthermore, the computed P–η curve is in good agreement with the experimental results, especially in the post-peak softening stage, when the nonlinear behavior is governed by the bridging effect of the pins across the crack.

It should also be noted that the proposed three-stage model includes experimentally calibrated input parameters, particularly the equivalent s_t–ε^* relationship derived from the pullout tests and the reduction factor

17517648, 0, Downloaded from https://onlinelibrary.wiley.com/doi/10.1002/suco.70706 by Politecnico Di Torino Sist. Bibl Del Polit Di Torino, Wiley Online Library on [30/07/2026]. See the Terms and Conditions (https://onlinelibrary.wiley.com/terms-and-conditions) on Wiley Online Library for rules of use; OA articles are governed by the applicable Creative Commons License

ψ_j. Since these parameters are based on a limited experimental dataset, the applicability of the proposed model to design R3DCP beams should be further examined through statistical analysis of the input parameters, for example, the bond–slip response of the pin-matrix interaction. Further experimental investigations, with a larger number of specimens, are required to confirm the robustness and general applicability of the proposed approach.

Finally, the beam specimens used in this study should be regarded as a controlled test configuration for evaluating the tensile bridging contribution of automatically inserted pins. Other tests are also necessary to clarify the behavior of pin reinforcement under different states of stress and loading conditions, in order to extend the applicability of R3DCP to a wider range of structures, including wall and shell-type elements.

NOTATIONS

A_{ci}	the area of the i-th concrete stripe in RC cross-section
A_p	cross-sectional area of the pin
A_{sj}	the area of the j-th reinforcement layer in RC cross-section
E_c	elastic modulus of concrete
E_s	elastic modulus of steel
F	applied load in pullout test
f_c	compressive strength of concrete
f_{ct}	tensile strength of concrete
f_u	ultimate strength of pin reinforcement
f_y	yield strength of pin reinforcement
k	number of groups composed by five laminated layers
k_1	slope of the ascending branch in the bilinear σ_t–ε^* relationship of the pins
k_2	slope of the descending branch in the bilinear σ_t–ε^* relationship of the pins
L	span length of a beam
l_1	the shortest embedded length of pin in a cracked beam
l_2	the longest embedded length of pin in a cracked beam
L_c	length of the softening region around a crack
l_e	embedded length of pin reinforcement in the pullout test
m	number of reinforcement layers in RC and R3DCP cross-sections
$M_a(z)$	bending moment distribution in a virtual beam
M, M_{max}	bending moment in a beam cross-section and its maximum value
N	axial load
n	number of concrete stripes in RC and R3DCP cross-sections
n_1, n_2, and n_3	number of pins with an efficiency of 100%, 60%, and 30%, respectively
P, P_{max}	applied load on real beam and its maximum value
q	self-weight on real beam
slip	relative displacement between pin reinforcement and cementitious matrix
U	applied concentrated load on a virtual beam
w	crack width
y_i	distance of the i-th concrete stripe from the X–Z plane
y_j	distance of the j-th reinforcement layer from the X–Z plane
ε	strain
ε^*	equivalent strain of the equivalent stress–strain relationship of pins
ε_{ci}	strain in the i-th concrete stripe of RC and R3DCP cross-sections
ε_{sj}	strain in the j-th reinforcement layer of RC and R3DCP cross-sections
η	deflection of a beam in bending
λ	strain in a cross-section at $y = 0$
σ	axial stress
σ_{ci}	stress in the i-th concrete stripe of RC and R3DCP cross-sections
σ_p	maximum stress in the ideal σ_t–ε^* relationship of the pins
σ_{sj}	stress in the j-th reinforcement layer of RC and R3DCP cross-sections
σ_t	equivalent stress in the pullout test
χ	cross-sectional curvature
$\chi_b(z)$	distribution of the cross-sectional curvature in a real beam
χ_p	curvature at the peak of bending moment in the M–χ diagram
ψ_j	reduction factor for the reinforcing contribution of pin at j-th reinforcement layer

AUTHOR CONTRIBUTIONS

Conceptualization: **TN** and **KO**; Methodology: **TN**, **APF**, **RE**, and **KO**; Investigation, **HT**, **NK**, **TA**, and **RE**; Validation: **TN**, **APF**, **YD**, and **KO**; Writing—original draft: **HT**, **NK**, and **TA**; Writing—review and editing: **TN**, **APF**, **YD**, and **KO**; Funding acquisition: **TN**, **YD**, and **KO**; Resources: **TN**, and KO; Supervision: TN, APF, and KO.

ACKNOWLEDGMENTS

The authors would like to express their sincere gratitude to Mr. Hideyuki Kajita and Mr. Yuki Miyazawa of Maeda Corporation for granting access to the 3D concrete printing

17517648, 0, Downloaded from https://onlinelibrary.wiley.com/doi/10.1002/suco.70706 by Politecnico Di Torino Sist. Bibl Del Polit Di Torino, Wiley Online Library on [30/07/2026]. See the Terms and Conditions (https://onlinelibrary.wiley.com/terms-and-conditions) on Wiley Online Library for rules of use; OA articles are governed by the applicable Creative Commons License

system, which enabled the fabrication of the specimens tested in this study. This work was also supported by Japan Society for the Prmotion of Science KAKENHI Grant Number JP23KF0004 and the Maeda Engineering Foundation. Open access publishing facilitated by Politecnico di Torino, as part of the Wiley - CRUI-CARE agreement.

DATA AVAILABILITY STATEMENT

The data that support the findings of this study are available from the corresponding author, upon reasonable request.

ORCID

Haruto Tasaki https://orcid.org/0009-0008-1964-4136
Noriyuki Kobayashi https://orcid.org/0009-0007-2860-5254
Tomoya Asakawa https://orcid.org/0009-0001-1253-8540
Alessandro P. Fantilli https://orcid.org/0000-0003-0383-7191
Yao Ding https://orcid.org/0000-0002-6654-0996
Ryo Egawa https://orcid.org/0009-0002-4549-1619
Kazunori Ohno https://orcid.org/0000-0003-3958-2901
Tomoya Nishiwaki https://orcid.org/0000-0001-6745-3141

REFERENCES

1. Bos F, Wolfs R, Ahmed Z, Salet T. Additive manufacturing of concrete in construction: potentials and challenges of 3D concrete printing. Virtual Phys Prototyp. 2016;11(3):209–25. https://doi.org/10.1080/17452759.2016.1209867
2. Nguyen-Van V, Li S, Liu J, Nguyen K, Tran P. Modelling of 3D concrete printing process: a perspective on material and structural simulations. Addit Manuf. 2023;61:103333. https://doi.org/10.1016/j.addma.2022.103333
3. Nematollahi B, Xia M, Sanjayan J. Current Progress of 3D concrete printing technologies. 34th International Symposium on Automation and Robotics in Construction (ISARC). Bratislava, Slovakia: International Association for Automation and Robotics in Construction (IAARC); 2017. p. 260–7. https://doi.org/10.22260/ISARC2017/0035
4. Vantyghem G, Corte WD, Shakour E, Amir O. 3D printing of a post-tensioned concrete girder designed by topology optimization. Autom Constr. 2020;112:103084. https://doi.org/10.1016/j.autcon.2020.103084
5. Yang W, Wang L, Ma G, Feng P. An integrated method of topological optimization and path design for 3D concrete printing. Eng Struct. 2023;291:116435. https://doi.org/10.1016/j.engstruct.2023.116435
6. Barbosa MS, dos Anjos MAS, Cabral KC, Dias LS. Development of composites for 3D printing with reduced cement consumption. Construct Build Mater. 2022;341:127775. https://doi.org/10.1016/j.conbuildmat.2022.127775
7. Wolfs RJM, Bos FP, Salet TAM. Hardened properties of 3D printed concrete: the influence of process parameters on interlayer adhesion. Cem Concr Res. 2019;119:132–40. https://doi.org/10.1016/j.cemconres.2019.02.017
8. Ting GHA, Quah TKN, Lim JH, Tay YWD, Tan MJ. Extrudable region parametrical study of 3D printable concrete using recycled glass concrete. J Build Eng. 2022;50:104091. https://doi.org/10.1016/j.jobe.2022.104091
9. Chen Y, Figueiredo SC, Li Z, Chang Z, Jansen K, Çopuroğlu O, et al. Improving printability of limestone-calcined clay-based cementitious materials by using viscosity-modifying admixture. Cem Concr Res. 2020;132:106040. https://doi.org/10.1016/j.cemconres.2020.106040
10. Bhattacherjee S, Basavaraj AS, Rahul AV, Santhanam M, Gettu R, Panda B, et al. Sustainable materials for 3D concrete printing. Cem Concr Compos. 2021;122:104156. https://doi.org/10.1016/j.cemconcomp.2021.104156
11. Jayathilakage R, Rajeev P, Sanjayan JG. Yield stress criteria to assess the buildability of 3D concrete printing. Construct Build Mater. 2020;240:117989. https://doi.org/10.1016/j.conbuildmat.2019.117989
12. Chang Z, Xu Y, Chen Y, Gan Y, Schlangen E, Šavija B. A discrete lattice model for assessment of buildability performance of 3D-printed concrete. Comput Concr Eng. 2021;36(5):638–55. https://doi.org/10.1111/mice.12700
13. Asensio J, Josa I, Monserrat A, de la Fuente A. 3D-printed concrete footbridges: an approach to assess the sustainability performance. Struct Concr. 2023;24:7705–25. https://doi.org/10.1002/suco.202201227
14. He L, Pan J, Hee YS, Chen H, Li LG, Panda B, et al. Development of novel concave and convex trowels for higher interlayer strength of 3D printed cement paste. Case Stud Constr Mater. 2024;21:e03745. https://doi.org/10.1016/j.cscm.2024.e03745
15. Buswella RA, Leal de Silva WR, Jones SZ, Dirrenberger J. 3D printing using concrete extrusion: a roadmap for research. Cem Concr Res. 2018;112:37–49. https://doi.org/10.1016/j.cemconres.2018.05.006
16. Bischof P, Mata-Falcon J, Ammann R, Näsbom A, Kaufmann W. Digitally fabricated weak interfaces to reduce minimum reinforcement in concrete structures. Struct Concr. 2023;24:1835–55. https://doi.org/10.1002/suco.202200732
17. Thajeel MM, Sólyom S, Balázs GL. Impact of printing directions and printing paths on the compressive strength of 3D printed concrete. Építőanyag – J Silicate Based Compos Mater. 2024;76(1):31–8. https://doi.org/10.14382/epitoanyag-jsbcm.2024.4
18. Mechtcherine V, Buswell R, Kloft H, Bos FP, Hack N, Wolfs R, et al. Integrating reinforcement in digital fabrication with concrete: a review and classification framework. Cem Concr Compos. 2021;119:103964. https://doi.org/10.1016/j.cemconcomp.2021.103964
19. Marchment T, Sanjayan J. Mesh reinforcing method for 3D concrete printing. Autom Constr. 2020;109:102992. https://doi.org/10.1016/j.autcon.2019.102992
20. Asakawa T, Nishiwaki T, Ohno K, Yokoyama S, Okada Y, Kojima S, et al. Fundamental study on automated interlayer reinforcing system with metal fiber insertion for 3D concrete printer. Third RILEM International Conference on Concrete and Digital Fabrication. Cham: Springer International Publishing; 2022. p. 411–6. https://doi.org/10.1007/978-3-031-06116-5_61

17517648, 0, Downloaded from https://onlinelibrary.wiley.com/doi/10.1002/suco.70706 by Politecnico Di Torino Sist. Bibl Del Polit Di Torino, Wiley Online Library on [30/07/2026]. See the Terms and Conditions (https://onlinelibrary.wiley.com/terms-and-conditions) on Wiley Online Library for rules of use; OA articles are governed by the applicable Creative Commons License

21. Marchment T, Sanjayan J. Lap joint reinforcement for 3D concrete printing. J Struct Eng. 2022;148(6):04022063. https://doi.org/10.1061/(ASCE)ST.1943-541X.0003361
22. Nishiwaki T, Miyata Y, Furue S, Fukatsu S, Kajita H. Reinforcing interlayers of three-dimensional-printed mortar using metal fiber insertion. ACI Mater J. 2021;118(6):331–40. https://doi.org/10.14359/51733133
23. Gebhard L, Mata-Falcon J, Anton A, Dillenburger B, Kaufmann W. Structural behaviour of 3D printed concrete beams with various reinforcement strategies. Eng Struct. 2021;240:112380. https://doi.org/10.1016/j.engstruct.2021.112380
24. Miyata Y, Asakawa T, Miyazawa Y, Nishiwaki T. Development and evaluation of high-strength fiber-reinforced cementitious composites applicable to concrete 3D printing systems. Proc Jpn Concr Inst. 2022;44(1):1558–63. (in Japanese).
25. Hambach M, Volkmer D. Properties of 3D-printed fiber-reinforced Portland cement paste. Cem Concr Compos. 2017;79:62–70. https://doi.org/10.1016/j.cemconcomp.2017.02.001
26. Egawa R, Nezu S, Nishijo K, Ohno K, Kojima S, Okada Y, et al. Different sized metal reinforcement insertion system using cartridge replacement mechanism for 3D concrete printer. Digital Concrete, Supplementary Proceedings. Braunschweig, Germany: Technische Universität Braunschweig; 2024. https://doi.org/10.24355/dbbs.084-202408201101-0
27. Tasaki H, Asakawa T, Kobayashi N, Nishiwaki T, Egawa R, Kojima S, et al. Direction-independent reinforcement by combination of fiber reinforced cementitious composite and automated pin insertion. 4th RILEM international conference on concrete and digital fabrication. Volume 53. Cham, Switzerland: Springer; 2024. p. 335–41. https://doi.org/10.1007/978-3-031-70031-6_39
28. Kobayashi N, Asakawa T, Nishiwaki T, Egawa R, Kojima S, Okada Y, et al. An automated pin insertion method for 3DCP and its reinforcement effects on beam specimens. Digital Concrete, Supplementary Proceedings. Braunschweig, Germany: Technische Universität Braunschweig; 2024. https://doi.org/10.24355/dbbs.084-202408201050-0
29. Marchment T, Sanjayan J. Reinforcement method for 3D concrete printing using paste-coated bar penetrations. Autom Constr. 2021;127:103694. https://doi.org/10.1016/j.autcon.2021.103694
30. International Federation for Structural Concrete. Advances on bond in concrete – state-of-the-art report, *fib* bulletin n. 106. Ostfildern-Kemnat, Germany: DCC Document Competence Center Siegmar Kästl e.K.; 2022. https://doi.org/10.35789/fib.BULL.0106
31. Fantilli AP, Mihashi H, Vallini P. Effect of bond-slip on the crack bridging capacity of steel fibers in cement-based. ASCE J Mater Civ Eng. 2008;20(9):588–98. https://doi.org/10.1061/(ASCE)0899-1561(2008)20:9(588)
32. International Federation for Structural Concrete. Model code 2010—final draft. fib Bulletin 65-66. Lausanne: fib; 2012. https://doi.org/10.1002/9783433604090
33. Fantilli AP, Orfeo B, Caldentey A. The deflection of reinforced concrete beams containing. Struct Concr. 2021;22:2089–104. https://doi.org/10.1002/suco.202000729
34. Fantilli AP, Mihashi H, Vallini P. Post-peak behavior of cement-based materials in compression. Mater J. 2007;104:501–10. https://doi.org/10.14359/18906
35. EN 1992-1-1:2004. Eurocode 2: design of concrete structures – part 1–1: general rules and rules for buildings. European Committee for Standardization. 2004.

AUTHOR BIOGRAPHIES



Haruto Tasaki, Department of Architecture and Building Science, School of Engineering, Tohoku University, Aoba 6-6-11-1209, Aramaki, Aoba-Ku, Sendai, Miyagi 980-8579, Japan. Email: tasaki.haruto.r6@dc.tohoku.ac.jp.



Noriyuki Kobayashi, Department of Architecture and Building Science, School of Engineering, Tohoku University, Aoba 6-6-11-1209, Aramaki, Aoba-ku, Sendai, Miyagi 980-8579, Japan. Email: noriyuki.kobayashi.r3@dc.tohoku.ac.jp.



Tomoya Asakawa, Technology Research Institute, Obayashi Corporation, Shimokiyoto 4-640, Kiyose, Tokyo 204-8558, Japan. Email: afiveotwo1380@gmail.com.



Alessandro P. Fantilli, Department of Structural, Building and Geotechnical Engineering, Politecnico di Torino, Corso Duca degli Abruzzi 24, 10129 Torino, Italy. Email: alessandro.fantilli@polito.it.



Yao Ding, School of Civil Engineering, Chongqing University, Shapingba District, Chongqing 400044, China. Email: dingyao@cqu.edu.cn.

17517648, 0, Downloaded from https://onlinelibrary.wiley.com/doi/10.1002/suco.70706 by Politecnico Di Torino Sist. Bibl Del Polit Di Torino, Wiley Online Library on [30/07/2026]. See the Terms and Conditions (https://onlinelibrary.wiley.com/terms-and-conditions) on Wiley Online Library for rules of use; OA articles are governed by the applicable Creative Commons License



Ryo Egawa, Graduate School of Information Science, Tohoku University, Aoba 6-3, Aramaki, Aoba, Sendai, Miyagi 980-8579, Japan. Email: egawa.ryo@rm.is.tohoku.ac.jp.



Kazunori Ohno, Tough Cyberphysical AI Research Center, Tohoku University, Aoba 468-1, Aramaki, Aoba, Sendai, Miyagi 980-0845, Japan. Email: kazunori@rm.is.tohoku.ac.jp.



Tomoya Nishiwaki, School of Engineering, Tohoku University, Aoba 6-6-11-1209, Aramaki, Aoba-ku, Sendai, Miyagi 980-8579, Japan. Email: tomoya.nishiwaki.e8@tohoku.ac.jp.

How to cite this article: Tasaki H, Kobayashi N, Asakawa T, Fantilli AP, Ding Y, Egawa R, et al. Testing and modeling reinforced 3D concrete printing. Structural Concrete. 2026. https://doi.org/10.1002/suco.70706

17517648, 0, Downloaded from https://onlinelibrary.wiley.com/doi/10.1002/suco.70706 by Politecnico Di Torino Sist. Bibl Del Polit Di Torino, Wiley Online Library on [30/07/2026]. See the Terms and Conditions (https://onlinelibrary.wiley.com/terms-and-conditions) on Wiley Online Library for rules of use; OA articles are governed by the applicable Creative Commons License